J. Fluid Mech. (2008), *vol.* 608, *pp.* 337–356.
doi:10.1017/S0022112008002309 Printed in the United Kingdom

Flow-induced forces in sphere doublets

J. J. DERKSEN
Chemical & Materials Engineering Department, University of Alberta,
Edmonton, Alberta, T6G 2G6 Canada
jos@ualberta.ca

(Received 2 December 2007 and in revised form 24 April 2008)

Motivated by applications in solids formation and handling processes we numerically investigate the force and torque required for maintaining a fixed contact between two equally sized solid spheres immersed in fluid flow. The direct numerical procedure applied is based on solving the Navier–Stokes equations by means of the lattice-Boltzmann method, with no-slip conditions at the surfaces of the moving spheres. It is validated by means of the analytical results due to Nir & Acrivos (1973) for sphere doublets in creeping flow. Subsequently, doublets are released in turbulent flows. In these cases, the contact force and torque strongly fluctuate, with peak levels much higher than would follow from simple dimensional analysis. The force fluctuation levels have been quantified by a linear relation in the ratio of sphere radius over Kolmogorov length scale.

1. Introduction

In many processes involving solid-particle formation or solids handling, particles have a tendency to stick together. Moisture can form liquid bridges gluing powder particles (Gopalkrishnana, Manas-Zloczowera & Fekeb 2005). In crystallization processes crystals tend to agglomerate because of the supersaturated environment they are in (Hounslow *et al.* 2001; Hollander *et al.* 2001). Suspension polymerization processes go through a 'sticky-phase' with significant agglomeration levels (Guerrero-Sanchez *et al.* 2006). In colloidal systems Van der Waals interactions can induce agglomeration. In biological applications (e.g. blood flow) agglomeration is also highly relevant (Mody *et al.* 2005).

Sometimes agglomeration is wanted to effectively grow particles making separation easier, e.g. in cyclone separators (Obermair *et al.* 2005) or filtration processes. However it is also a mechanism that potentially destroys a narrow particle size distribution, and as a result could reduce product quality. Much effort goes into preventing or promoting agglomeration, and into repairing the harm agglomeration has done (e.g. in grinding and milling process steps, Kwade & Schwedes 2002). Whether agglomeration is wanted or unwanted, it is relevant to assess the stability and the integrity of the bond holding the primary particles together. Agglomerates can break as a result of a variety of mechanisms: collisions with other particles or with the interior of a process vessel; dissolution of their bond due to a changing chemical environment; change of particle surface properties. Also the flow of fluid surrounding an agglomerate is a potentially destabilizing factor: Velocity gradients induce forces on and in agglomerates that could make them break.

Understanding and modelling breakage as a result of fluid flow is largely based on relatively simple concepts involving estimating shear rates and semi-empirical correlations for breakage statistics. In recent papers on the broader subject of population balance modelling of colloidal dispersions (Soos, Sefcik & Morbidelli 2006; Marchisio *et al.* 2006), the physical descriptions of breakage due to flow date back quite some time (Delichatsios & Probstein 1976; Kusters 1991), and are subject to refinement in terms of improving the (statistics of the) hydrodynamic environment of agglomerates, and in terms of estimating the hydrodynamic forces in agglomerates immersed in complex flow.

In turbulent flows, the shear (or more properly rate of strain) experienced by an agglomerate is strongly fluctuating. Given the suspected nonlinear coupling between rate of strain and breakage probability, working with an average (in time and/or space) or effective rate of strain is a critical simplification. Furthermore, agglomerates with sizes comparable to or bigger than the smallest turbulent scales (these typically are non-colloidal but still can be sub-millimetre-size agglomerates) do not experience homogeneous rate of strain. The deformation rate varies over their surface. This influences the forces in (and on) the agglomerate induced by the flow.

With the above in mind it is clear that it is impossible to formulate a generic way of estimating the flow-induced forces in agglomerates. The parameter space is simply too large. The morphology of the agglomerate, the shape of the primary particles, the material properties of the solid and liquid involved, and the structure of the flow at the scale of the agglomerate all play their role. Focusing on the fluid dynamics, we specifically anticipate complications when the smallest flow scales are comparable to or smaller than the size of the agglomerate. In this case the flow around the agglomerate is inhomogeneous and cannot be characterized by a single shear rate, or a single rate-of-strain tensor. What can be done, however, is to assess the role of the non-ideal factors in the flow-induced forces in agglomerates. For this I have chosen to first consider virtually the simplest agglomerate possible: two equally sized spheres, rigidly constrained together at their (single) point of contact. The two spheres are touching; they have zero separation. There is sufficient reason for considering this simple case first. It allows us to develop and test a methodology based on numerical simulation of the fluid flow around the agglomerate, and the way the agglomerate responds to the flow. The specific case of a sphere doublet allows validation of the numerical procedure against analytical results due to Nir & Acrivos (1973) who considered the creeping motion of two touching spheres in a linear shear field. After validating our numerical procedure, we release sphere doublets in turbulent flow with flow structures of a size comparable to the size of the spheres, and with Reynolds numbers (based on sphere size and slip velocities, or based on (local) deformation rates) well above unity, i.e. a situation beyond the validity of Nir & Acrivos' analytical approach. We show highly intermittent behaviour of the force needed to hold the two spheres together. The peaks in this force are typically one order of magnitude higher than the force one would estimate based on an effective turbulent shear (e.g. $\dot{\gamma} = \sqrt{\varepsilon/\nu}$ with ε the energy dissipation rate, and ν the kinematic viscosity).

The aim of this paper is to present and validate a numerical procedure for calculating flow-induced internal forces in agglomerates, and to show the level of these forces as a function of turbulence intensity. The motivation is using the insights gained to devise breakage models, and for the design of process equipment where breaking (or not breaking) agglomerates is critical.

The organization of this paper is as follows. We first describe our computational methodology which is based on directly solving the motion of a sphere doublet and the fluid in its vicinity (the latter with the lattice-Boltzmann method). We do not consider actual breakage of the doublets. Instead we determine at all times the forces and torques needed to maintain the bond between the spheres. We subsequently discuss simulations of a doublet in a simple shear field at low Reynolds number. Results of these simulations are compared to the analytical results due to Nir & Acrivos (1973), and show good agreement. Then we immerse the doublet in turbulent fields, keep track of the forces and torques in the doublet, and interpret the results. The final section summarizes the main conclusions.

2. Numerical methodology

In the simulations, two spheres attached to one another are placed in a liquid-filled domain. The motion of the spheres and the liquid are fully coupled, i.e. the fluid flow sets the sphere doublet in motion; the motion of the sphere doublet on its turn induces fluid flow. We solve the fluid flow with the lattice-Boltzmann method (LBM). For flows in complexly shaped domains and/or with moving boundaries, this method has proven its usefulness (see e.g. the review article by Chen & Doolen 1998). In the LBM, the computational domain is discretized into a number of lattice nodes on a uniform, cubic grid. Fluid parcels move from each node to its neighbours according to prescribed rules. It can be proven by means of a Chapman–Enskog expansion that, with the proper grid topology and collision rules, this system obeys, in the low Mach number limit, the incompressible Navier–Stokes equations (Chen & Doolen 1998; Succi 2001). The specific implementation used in our simulations has been described by Somers (1993), which is a variant of the widely used lattice BGK scheme to handle the collision integral (e.g. see Qian, d'Humieres & Lallemand 1992). We use the scheme due to Somers, as it manifests a more stable behaviour at low viscosities compared to LBGK. A lattice-Boltzmann fluid is a compressible fluid. In order to mimic incompressible flow, as is done in this paper, the Mach number must be sufficiently low. In the simulations presented here the local Mach number never exceeded 0.04.

The fluid flow and the motion of the spheres are coupled by demanding that at the surface of each of the two spheres forming the doublet the fluid velocity matches the local velocity of the surface (that is the sum of the linear velocity $\boldsymbol{v}_p$ and $\boldsymbol{\Omega}_p \times (\boldsymbol{r}-\boldsymbol{r}_p)$ with $\boldsymbol{\Omega}_p$ the angular velocity of the sphere, $\boldsymbol{r}_p$ the centre position of the sphere, and $\boldsymbol{r}$ a point on its surface); in the forcing scheme that is applied here this is accomplished by imposing additional forces on the fluid at the surface of the solid sphere (which are then distributed to the lattice nodes in the vicinity of the particle surface). The details of the implementation can be found elsewhere (Goldstein, Handler & Sirovich 1993; Derksen & Van den Akker 1999; Ten Cate *et al.* 2002). The collection of forces acting on the fluid at the sphere's surface and its interior is subsequently used to determine the hydrodynamic force and torque acting on the sphere (action = −reaction) (Derksen & Sundaresan 2007).

In our simulations, the radius of each spherical particle is specified and input radius refers to this radius scaled by the lattice spacing. In the LBM simulations, as the spherical particle is represented by forces that are confined to a cubic grid, the input radius does not reflect the actual radius of the particle. A calibration procedure to estimate the effective radius of this object (commonly referred to as the hydrodynamic radius) was introduced by Ladd (1994). We apply his scheme to estimate the hydrodynamic radius of the particles. The hydrodynamic radius is denoted as a and is given in lattice units. In this study radii in the range $a = 6$–12 have been used. Typically the input radius turns out to be some 10% smaller than the hydrodynamic radius.

At this stage of the simulation procedure, the two spheres forming the doublet are considered independent entities. For each sphere we determine the hydrodynamic force ($\boldsymbol{F}_{h1}$ and $\boldsymbol{F}_{h2}$), and torque ($\boldsymbol{T}_{h1}$ and $\boldsymbol{T}_{h2}$) acting on it. In order to maintain the contact point, we introduce an interaction force $\boldsymbol{F}_i$, and interaction torque $\boldsymbol{T}_i$, acting at the contact point. The convention taken here is that the force $\boldsymbol{F}_i$ acts on sphere 1, and $-\boldsymbol{F}_i$ acts on sphere 2. Similarly $\boldsymbol{T}_i$ acts on sphere 1, $-\boldsymbol{T}_i$ on sphere 2. The conditions to maintain the contact point between the spheres provide the equations to solve for $\boldsymbol{F}_i$ and $\boldsymbol{T}_i$. These conditions are

$$\frac{\mathrm{d}\boldsymbol{v}_{c1}}{\mathrm{d}t} = \frac{\mathrm{d}\boldsymbol{v}_{c2}}{\mathrm{d}t} \quad \text{and} \quad \boldsymbol{\Omega}_{p1} = \boldsymbol{\Omega}_{p2} \equiv \boldsymbol{\Omega}_p \tag{1}$$

with

$$\boldsymbol{v}_{c1} = \boldsymbol{v}_{p1} + \tfrac{1}{2}\boldsymbol{\Omega}_{p1} \times \boldsymbol{\Delta r} \quad \text{and} \quad \boldsymbol{v}_{c2} = \boldsymbol{v}_{p2} - \tfrac{1}{2}\boldsymbol{\Omega}_{p2} \times \boldsymbol{\Delta r} \tag{2}$$

the velocity of the contact point from the perspective of sphere 1 and sphere 2 respectively. The vector $\boldsymbol{\Delta r}$ connects the centres of the two spheres. Equation (1) provides the six conditions to solve the (in total six) components of $\boldsymbol{F}_i$ and $\boldsymbol{T}_i$. In the Appendix we give the derivation for solving $\boldsymbol{F}_i$ and $\boldsymbol{T}_i$ in full detail.

Once the interaction force and torque have been determined, we know the total force and torque on each of the two spheres, and numerically solve their equations of linear and rotational motion. The updated sphere velocities and positions are then communicated to the fluid flow part of the simulation procedure and used to solve for the fluid flow in the next time step; and so on.

We have chosen an approach involving solving for the motion of the two spheres separately, instead of solving the equation of motion for a sphere doublet as a whole, as the former directly provides us with the interaction force and torque. Since these are necessary to maintain the integrity of the doublet, they can be directly compared to the strength of a bond in order to assess if the flow would be able to break the bond.

Verification: creeping flow

In a seminal article, Nir & Acrivos (1973) analytically solved the problem of the motion of a sphere doublet (with each sphere of arbitrary size) in a linear shear field at creeping flow conditions. Their analysis includes the force acting on the spheres. The expression for the force $\boldsymbol{F}_{NA}$ (components $F_{NA\alpha}$, $\alpha = x, y, z$) exerted on one of the two spheres that they give is

$$F_{NA\alpha} = \pi\mu a^2 (h_1 e_{\alpha\beta} p_\beta + h_2 e_{\gamma\beta} p_\gamma p_\beta p_\alpha) \tag{3}$$

with μ the dynamic viscosity of the working fluid. The force exerted on the other sphere has the same size and opposite direction. In (3) the parameters h_1 and h_2 are functions of the ratio of the radii of the spheres involved. In the case of two equally sized spheres $h_1 = 4.463$, and $h_2 = 7.767$. The vector $\boldsymbol{p}$ is the unit vector in the direction of the line connecting the two sphere centres ($\boldsymbol{p} = \boldsymbol{\Delta r}/|\boldsymbol{\Delta r}|$ in terms of figure 15 (in the Appendix));

$$e_{\alpha\beta} = \frac{1}{2}\left(\frac{\partial u_\alpha}{\partial x_\beta} + \frac{\partial u_\beta}{\partial x_\alpha}\right)$$

is the rate-of-strain tensor of the undisturbed flow field in which the doublet is immersed. For creeping flow the interaction force $\boldsymbol{F}_i$ is equivalent to $\boldsymbol{F}_{NA}$. We use this to verify our numerical procedure.

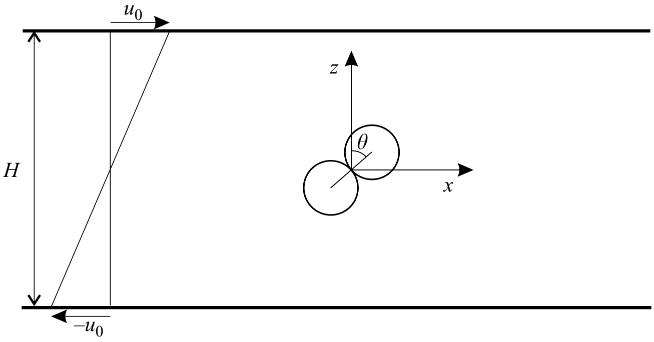

FIGURE 1. Doublet in simple shear flow. Shear is generated by moving two flat plates in opposite directions.

The case we single out is a doublet of equally sized spheres in a simple shear flow; see figure 1 (which also serves to define the coordinate system). If this doublet is placed with its separation vector $\boldsymbol{\Delta r}$ in the wall-normal direction (z-direction), it will start rotating about the y-axis. For this configuration the only non-zero components of the rate-of-strain tensor are $e_{xz} = e_{zx} = \frac{1}{2}\dot{\gamma}$ with $\dot{\gamma} \equiv 2u_0/H$. With $[p_x, p_y, p_z] = [\sin\theta, 0, \cos\theta]$ it follows from (3) that the analytical expression for the normal force (the component of the interaction force in the direction of the line connecting the sphere centres) $F^n_{NA} \equiv \boldsymbol{F}_{NA} \cdot \boldsymbol{p}$ in this case is

$$F^n_{NA} = \pi\mu\frac{a^2}{2}\dot{\gamma}\,(h_1 + h_2)\sin(2\theta) \tag{4}$$

where we have taken the convention of a tensile normal force being positive, and a compressive force negative. In the θ-range $0\ldots\frac{1}{2}\pi$ (modulo π) the normal force is tensile; for $\theta = \frac{1}{2}\pi\ldots\pi$ (modulo π) the normal force is compressive. Extreme values of the force occur at $\theta = \frac{1}{4}\pi$ (modulo $\frac{1}{2}\pi$).

Nir & Acrivos (1973) also give a general expression for the rotation rate of the doublet in a linear shear field. Applying this expression to the case of equally sized spheres in simple shear results in

$$\Omega_{py} = \frac{\mathrm{d}\theta}{\mathrm{d}t} = \frac{1}{2}\dot{\gamma}\,(1 + C\cos(2\theta)). \tag{5}$$

With C a constant equal to 0.594 (in the terminology of Nir & Acrivos $C = (r_e^2 - 1)/(r_e^2 + 1)$ with $r_e = 1.982$ for two equally sized spheres). Given the choice of the coordinate system and geometry, Ω_{py} is always positive, with minimum rotation rate when the doublet is aligned with the flow, and maximum rotation rate when perpendicular to the flow.

In the numerical simulations we consider a flow domain with size $nx \times ny \times nz$ in the x-, y-, and z-direction respectively. The upper and lower walls ($z = 0$ and $z = nz$) are no-slip walls with respective velocities $-u_0$ and u_0 in the x-direction. As a result $\dot{\gamma} = 2u_0/nz$. The conditions at the other bounding walls are periodic. In the centre of this domain we place a doublet consisting of two equally sized spheres with radius a. We define the Reynolds number as $Re = \dot{\gamma}a^2/\nu$; in order to compare with the analytical solution we demand $Re \ll 1$ (creeping flow). The solid over fluid density ratio is kept constant at $\rho_s/\rho_f = 4.0$.

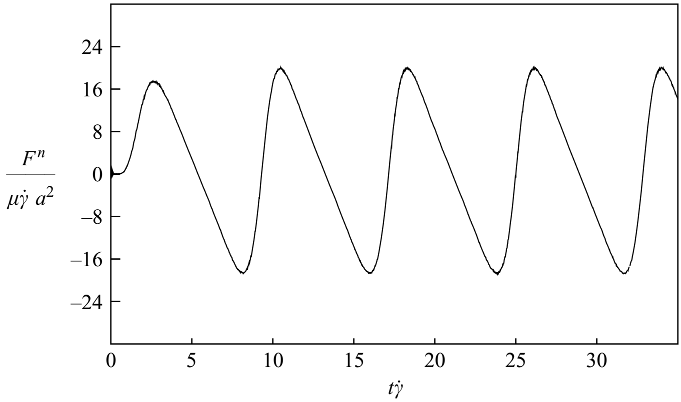

FIGURE 2. Interaction force in the normal direction (F^n) as a function of time. The parameters for this simulation are: $a = 6$, $nx \times ny \times nz = 96 \times 144 \times 144$, $Re = 0.06$.

At time $t = 0$ (the doublet then has a $\theta = 0$ orientation) we start moving the upper and lower plates. A time series of the normal component of the interaction force is given in figure 2. We see that after a short startup phase, the force fluctuates in a periodic manner with constant amplitude. The slight noise in the force signal is due to the fixed grid over which the spherical particles move; higher spatial resolution reduces this noise (see also Ten Cate *et al.* 2002). Plotting the force as a function of the doublet orientation θ as is done in figure 3 allows a direct comparison with the analytical result as given in (4). In figure 3(*a*), we plot our 'raw' computational signal along with the analytical result. This signal contains a startup part with reduced force amplitude. Once the signal is steady, we observe good agreement with the analytical result. The agreement improves if we correct for the centrifugal force as shown in figure 3(*b*). Here we have subtracted an amount $m\Omega_{py}^2 a$ (with $m = \frac{4}{3}\pi\rho_s a^3$ the mass of one sphere) from the computed force in the normal direction, with the instantaneous value of Ω_{py} taken from the simulations. The phase shift between simulation and analytical results is approximately 0.015π; the deviation in amplitude of the corrected (for the centrifugal force) computational result from the analytical result is approximately 1 %. It should be noted that the results shown above require sufficiently large spacing nz between the two bounding walls, see figure 4. For $nz \geqslant 90$ the force amplitude is practically independent of nz for spheres with $a = 6$.

We speculate that the small difference between the analytical and numerical result as observed in figure 3(*b*) is due to finite Reynolds number effects, with the Saffman lift force (Saffman 1965, 1968) playing a significant role since it is proportional to $\sqrt{Re}$. In the current configuration the Saffman lift force is strongest if the doublet is at the $\theta = 0$ (modulo π) orientation since then the slip velocity in the direction of the shear field is highest. At this orientation the doublet's rotation rate is $\Omega_{py} = \frac{1}{2}\dot{\gamma}(1 + C) \approx 0.8\dot{\gamma}$ (see (5)). As a result, the slip velocity (defined as the fluid velocity of the undisturbed shear flow at the sphere centre minus the sphere velocity) of the upper sphere is $V \approx 0.2\dot{\gamma}a$, and of the lower sphere it is $V \approx -0.2\dot{\gamma}a$. An estimate of the Saffman force (based on the single-sphere Saffman expression) then is

$$F_{Sl,\theta=0} = 6.46 \cdot 0.2\mu a^2\dot{\gamma}\sqrt{Re} = 1.29\mu a^2\dot{\gamma}\sqrt{Re}. \qquad (6)$$

On the upper sphere it acts in the positive z-direction and on the lower sphere in the negative z-direction, and thus results in an extra tensile (positive) interaction force.

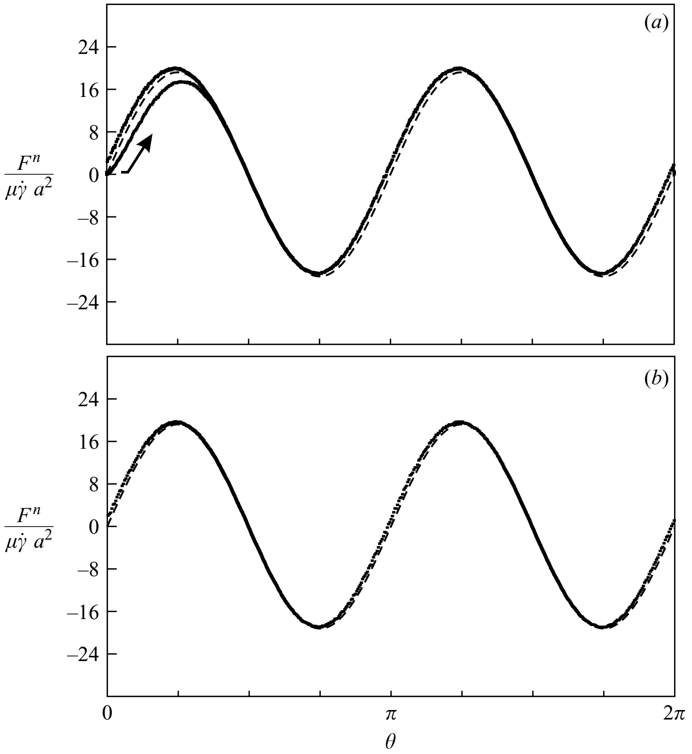

FIGURE 3. Interaction force in the normal direction (F^n) as a function of the orientation angle θ of the doublet. Same parameters as in figure 2. (*a*) Closely spaced symbols: numerical results; dashed curve: analytical result (4). The arrow indicates the starting point of the simulation and the direction in which it evolves. (*b*) Closely spaced symbols: numerical results in fully developed flow corrected for the centrifugal force; dashed curve: analytical result (4).

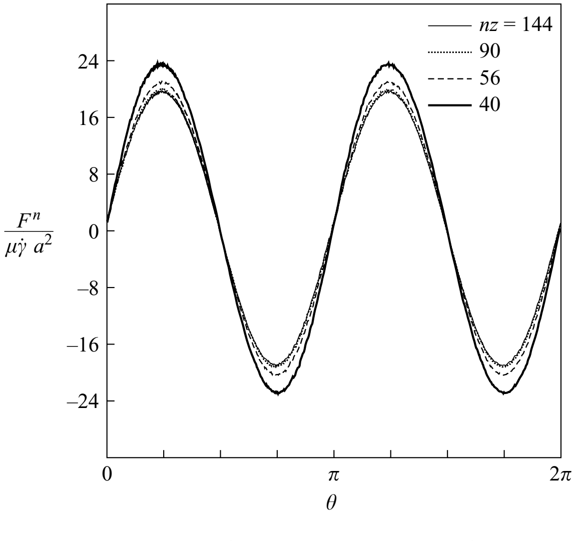

FIGURE 4. Interaction force F^n (corrected for centrifugal effects) as a function of θ ; influence of the domain size in the z-direction. Thin curve: same as results shown in figure 3*b* ($nz = 144$); dotted curve: $nz = 90$; dashed curve: $nz = 56$; thick curve: $nz = 40$.

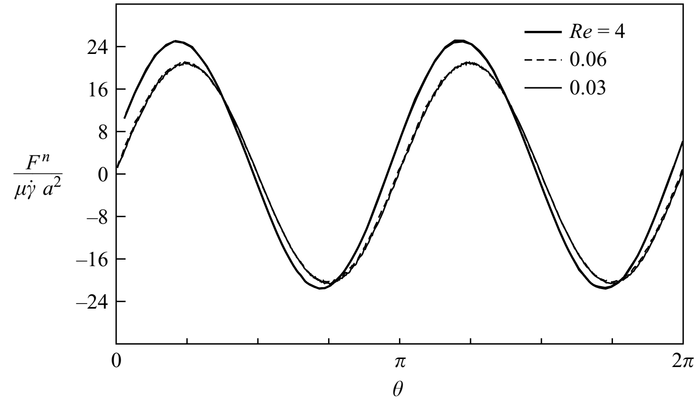

FIGURE 5. Interaction force F^n (corrected for centrifugal effects) as a function of θ; influence of the Reynolds number. $a = 6$, $nx \times ny \times nz = 96 \times 56 \times 56$.

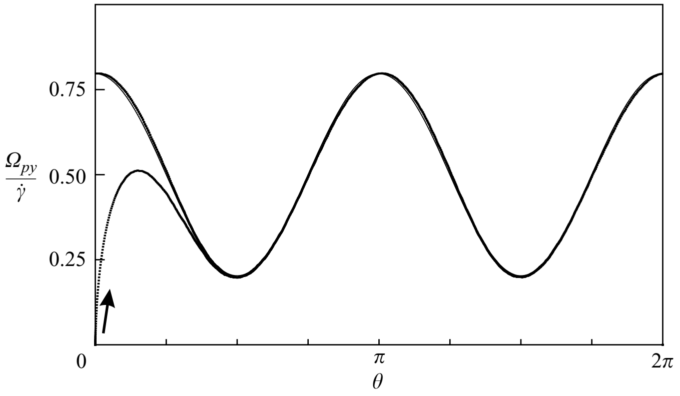

FIGURE 6. Rotation rate of the doublet along the y-axis as a function of the orientation angle θ. Same simulation parameters as in figure 2. Closely spaced symbols: numerical results; curve: analytical result (5). The arrow indicates the starting point of the simulation and the direction in which it evolves. $a = 6$, $nx \times ny \times nz = 96 \times 144 \times 144$, $Re = 0.06$.

In figure 5 we show results for three different Reynolds numbers. We see a small reduction of the tensile force (corrected for centrifugal effects) at $\theta = 0$ (modulo π) if we reduce Re from 0.06 to 0.03. The values of the tensile force at $\theta = 0$ (modulo π) are $0.5\mu a^2\dot{\gamma}$ for $Re = 0.03$, and $0.9\mu a^2\dot{\gamma}$ for $Re = 0.06$ (with typically an accuracy of $0.1\mu a^2\dot{\gamma}$ given the slight noise in the force signal). The estimates of the Saffman force using (6) yield $0.22\mu a^2\dot{\gamma}$ and $0.32\mu a^2\dot{\gamma}$ for $Re = 0.03$ and 0.06 respectively. A significant portion of the tensile force at $\theta = 0$ (modulo π) can be attributed to Saffman lift. If we strongly increase the Reynolds number (to $Re = 4$), inertia induces a large phase shift and a clear top–bottom asymmetry (tensile forces getting much stronger than compressive forces), see again figure 5.

We checked the rotation rate as a function of θ at creeping flow conditions. After reaching fully developed state, the rotation rate along the y-axis as simulated agrees very well with the analytical result as expressed in (5), see figure 6.

Results presented so far are for a spatial resolution such that the sphere radius $a = 6$ lattice spacings. Taking $nz = 56$ and $Re = 0.06$ as a base case, we checked the impact of the spatial resolution by performing two additional simulations with $a = 8$

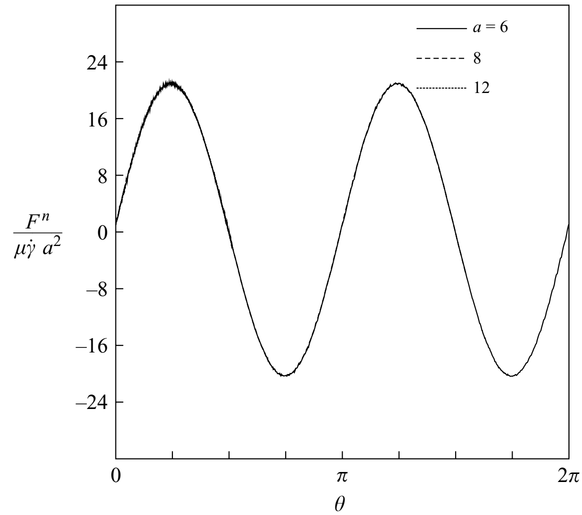

FIGURE 7. Interaction force F^n (corrected for centrifugal effects) as a function of θ; influence of the spatial resolution of the simulations in terms of a (the number of lattice spacings per particle radius). Conditions: see text.

and $a = 12$ while keeping the dimensionless numbers (aspect ratios, Reynolds number, and density ratio) the same as in the base case. The results in terms of the normal interaction force can hardly be distinguished, the major difference being the noise level that becomes smaller for higher resolution (see figure 7).

In conclusion this validation study shows good agreement between computational and analytical results, and grid independence for $a \geqslant 6$. It should be noted that in order to obtain these results we used the concept of a hydrodynamic radius, i.e. we calibrated the spheres such that a single sphere experiences the correct drag under creeping flow conditions. This has been a commonly used concept in this type of simulation since its introduction by Ladd (1994). In the remainder of this paper we will apply the computational procedure to study forces in sphere doublets immersed in turbulent flow, with the doublet size not small compared to the Kolmogorov length scale.

3. Doublets in turbulent flow

A single doublet consisting of two equally sized spheres is placed in a three-dimensional cubic fully periodic domain. The domain size is 128^3 lattice nodes. The spheres forming the doublet have radius $a = 6$ or $a = 8$ lattice spacings (in the previous section it was shown that such resolutions were sufficient for correctly resolving the interaction force in the doublet). We limit consideration to systems with a fixed solid over fluid density ratio $\rho_s/\rho_f = 4.0$. In the computational domain we create a homogeneous, isotropic turbulent flow by linear forcing (Rosales & Meneveau 2005). This flow is characterized by its time- and space- averaged energy dissipation rate $\bar{\varepsilon}$ and root-mean-square velocity u_{rms}. From these quantities measures for the Kolmogorov scales and relevant Reynolds numbers,

$$Re_{rms} = \frac{u_{rms}a}{\nu}, \quad Re_{\varepsilon} = \frac{a^2\sqrt{\bar{\varepsilon}/\nu}}{\nu}$$

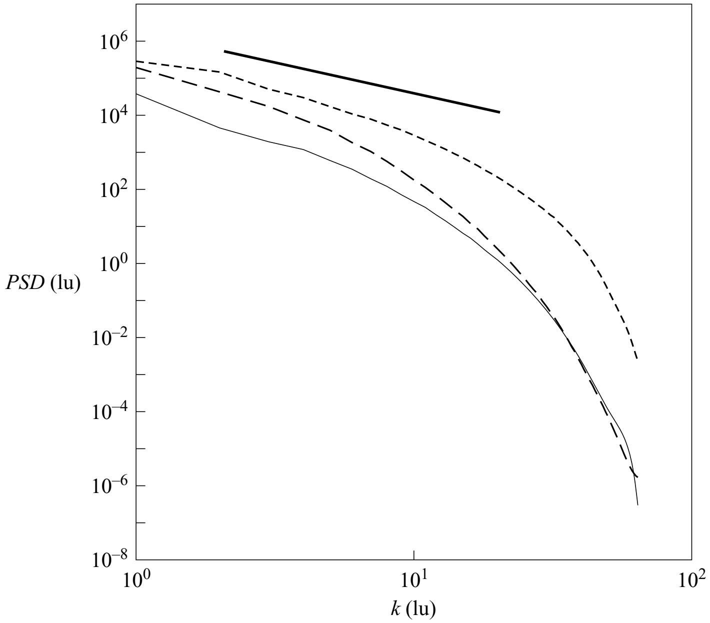

FIGURE 8. Power spectral density (PSD) as a function of wavenumber (both in lattice units) for three simulated cases, all on a 128^3 grid. Solid curve: $a/\eta_K = 2.1$ and $a = 6$, long-dashed curve $a/\eta_K = 6.1$ and $a = 8$, short-dashed curve $a/\eta_K = 16$ and $a = 8$. The thick line indicates the $-\frac{5}{3}$ slope.

are derived. Our main interest is in the effect non-uniform rate of that strain around the doublet has on the interaction force and torque. As the primary independent variable, therefore, the ratio a/η_K is considered, with the Kolmogorov length scale $\eta_K = (\nu^3/\bar{\varepsilon})^{1/4}$. In terms of this dimensionless variable we would like to cover as large a range as possible. Both at the low end and the high end we are, however, limited by computational restraints. At the high end of a/η_K there is a need for large computational domains, and large values of a (in terms of lattice spacings) to accurately resolve the flow around the spheres. At the low end we are limited by the need to resolve the spheres with at least $a = 6$ resolution (our methodology was validated for this resolution) implying the need for η_K significantly bigger than the lattice spacing and again the need for large overall domains to develop turbulent structures covering a significant range of scales. In this study a/η_K ranges roughly from 2 to 20. It should be acknowledged, however, that for the lower end of this range turbulence was not fully developed as can be seen from the spectra given in figure 8. At the high end of the range we approach the limits of properly resolving turbulence with the computational grid. At the highest a/η_K (being 21.4), we had $a = 8$ (lattice units) and thus $\eta_K = 0.37$. The maximum wavenumber resolved in the simulations is $k_{\max} = \pi$ (in lattice units). As a result $\eta_K k_{\max}$ is close to, but still above, 1 which is generally considered sufficient spatial resolution (see e.g. Overholt & Pope 1998).

As the doublet moves through the computational domain, we track its position and orientation, its linear and angular velocity, its direct hydrodynamic environment, and the interaction force and torque between the two spheres forming it. Typical time series for the normal force, the shear force (the projection of the interaction force on a plane normal to the vector connecting the two spheres), the torsion (the

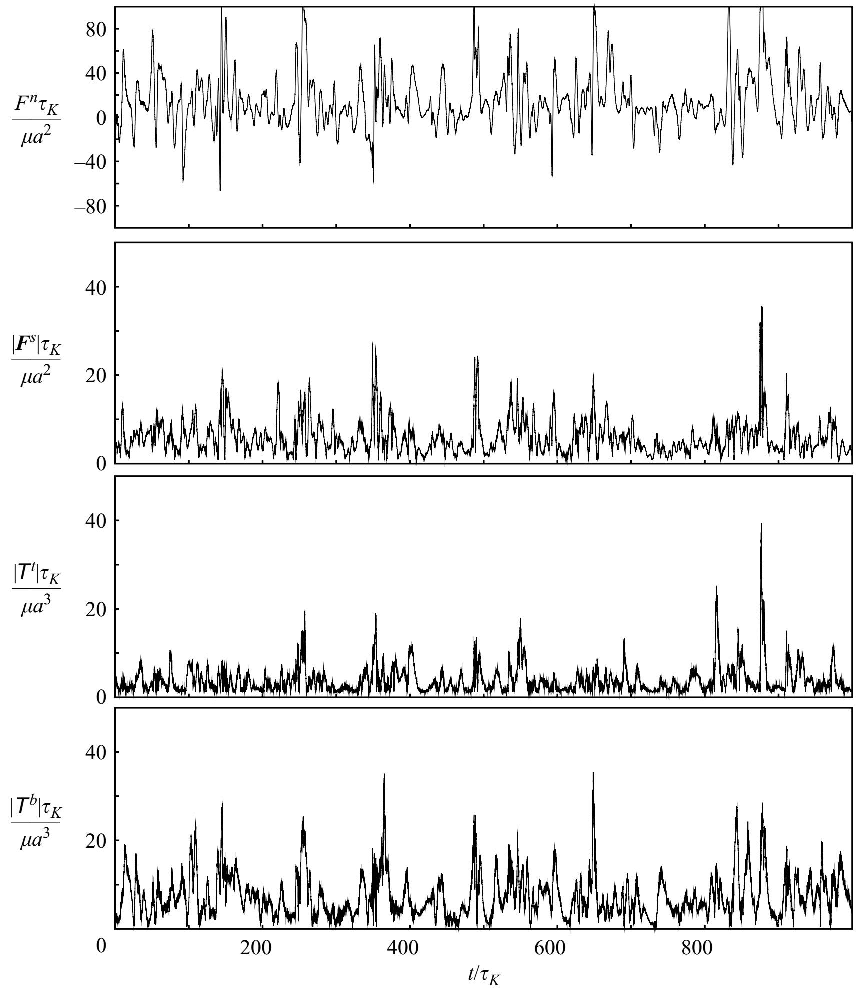

FIGURE 9. Time series of the interaction force F^n, the absolute value of the shear force $\boldsymbol{F}^s$, the absolute torsion $\boldsymbol{T}^t$, and the absolute bending torque $\boldsymbol{T}^b$ of a doublet in turbulent flow as a function of time. The turbulence conditions are such that $a/\eta_K = 8.3$, and $Re_{rms} = 27$. The resolution is such that $a = 8$.

torque along the vector connecting the two sphere centres), and bending torque are given in figure 9. We observe highly intermittent behaviour. Fluctuations have a time scale of $1-10$ times the Kolmogorov time $\tau_K = \sqrt{\nu/\varepsilon}$. In figure 9 the forces have been scaled in a manner consistent with the way we scaled the forces in simple shear (with $\dot{\gamma} = 1/\tau_K$). The time-averaged normal force is positive, i.e. tensile. As we will demonstrate below, this is partly due to the centrifugal force. The peak levels of the shear force are generally somewhat smaller than those of the normal force. Torsion and bending torque fluctuate at similar levels. Their frequencies are comparable to those of the force fluctuations.

In what follows, we will limit to the normal force, and the way it relates to the turbulence properties. A comprehensive description of the statistics of all force and torque components is beyond the scope and aim of this article which is to develop tools for demonstrating and quantifying the effects of the direct hydrodynamic environment

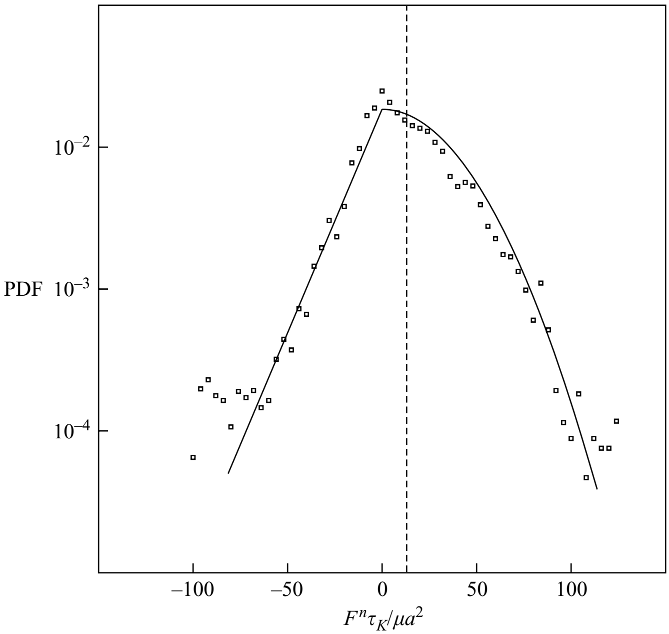

FIGURE 10. Probability density function (PDF) of the interaction force F^n. Symbols: computational results; curves: by-the-eye fits of an exponential distribution (straight line), and a Gaussian distribution (parabola). The dashed line indicates the average. The turbulence conditions are such that $a/\eta_K = 8.3$, and $Re_{rms} = 27$. The resolution is $a = 8$.

on forces in agglomerates. If we are considering a particular solid material for which the shear forces or torques are more critical for breakage, the methodology for determining their (statistical) behaviour is available.

The probability density function (PDF) for an extended version of the time series of the normal force as given in figure 9 is given in figure 10. It has an asymmetric shape. The decay on the negative side (compressive forces) is approximately linear on a linear-logarithmic scale (exponential decay). On the positive side (tensile forces) the decay fits a Gaussian fairly well. This is akin to the shape of the PDF of the relative radial velocity of two closely spaced points in a single- phase homogenous isotropic turbulent flow (Wang, Wexler & Zhou 2000; Ten Cate *et al.* 2004): Gaussian for positive (separating) radial velocities, and exponential for negative (approaching) velocities. The radial velocity PDF has its maximum for velocity values greater than zero, its average being zero by definition. The interaction force showing a similarly shaped PDF reflects velocity differences experienced by the two spheres causing differences in drag resulting in the interaction force.

We further reduce the normal force data by only considering the first two moments of its PDF, i.e. the average normal force and its standard deviation, where our main interest is in assessing and modelling the fluctuation levels. Averages were all taken over simulations running for 100 000 time steps. Measured in units of the Kolmogorov time scale, the minimum length of a simulation was $200\tau_K$. With respect to the typical time scale of the force fluctuations (of the order of τ_K to $10\tau_K$) this is sufficient. The extreme events as seen in figure 9, however, have much longer time intervals and make the estimates of the first and second moment uncertain. Running over significantly longer time spans would solve this problem but quickly becomes unpractical if we also

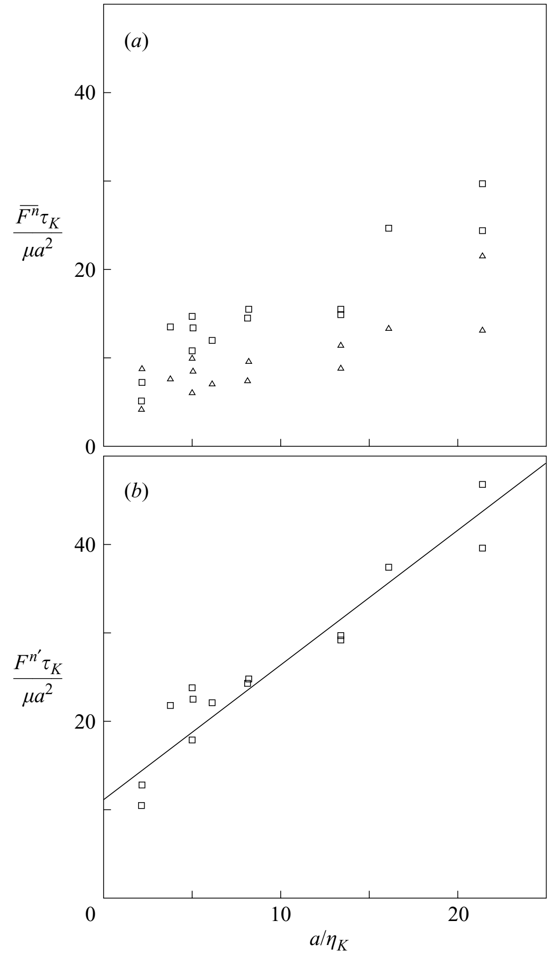

FIGURE 11. (*a*) Average $\overline{F^n}$ and (*b*) root-mean-square $F^{n'}$ normal force in the sphere doublet at various turbulence conditions, characterized by the ratio a/η_K. The square symbols in (*a*) are the total average normal force; the triangles indicate the contribution of the centrifugal force. The trend line in the bottom panel (equation (7)), see text) has intercept $\alpha = 11 \pm 2$ and slope $\beta = 1.5 \pm 0.2$.

want to capture a broad range of turbulence conditions (i.e. do many simulations). We have instead chosen to replicate a few 10^5 time-step simulations and this way assess the level of statistical uncertainty in the moments of the normal force PDF.

In figure 11(*a*) we plot the average force $\overline{F^n}$ scaled with $\mu a^2/\tau_K$ as a function of the ratio of the primary particle radius a over the Kolmogorov length scale $a/\eta_K = a(\bar{\varepsilon}/\nu^3)^{1/4}$ for a number of simulations. In the same figure we also plot the contribution of the centrifugal force to this average, the latter being equal to $\overline{F^c} = m\overline{|\boldsymbol{\Omega}_p|^2}a$. The average normal force data show significant scatter. Different points at the same a/η_K ratio are duplications, indicating the statistical contribution to the scatter. The overall trend is higher average forces for higher a/η_K ratios. The average normal force is systematically larger (by a factor 2 to 3 for $a/\eta_K > 5$) than the average centrifugal force. Apparently the latter cannot fully explain why the average normal force is always positive (tensile). An additional contribution to the average tensile force is probably due to the asymmetric shape of the PDF of the radial velocity, inducing an additional (on average) tensile force.

In figure 11(*b*) the standard deviation of the normal force ($F^{n'}$) is plotted. It shows a more consistent trend with a/η_K than the average force data. The standard deviation is generally larger than the average, making it more relevant for assessing doublet breakage. The computational data for the systems studied here roughly fit a linear function:

$$\frac{F^{n'}\tau_K}{\mu a^2} = \alpha + \beta\frac{a}{\eta_K} \tag{7}$$

with $\alpha = 11 \pm 2$ and $\beta = 1.5 \pm 0.2$. The intercept α is the root-mean-square normal force in the limit $a/\eta_K \to 0$. In this limit the doublet is immersed in a continuously changing linear shear field. For specific a this limit can only be reached by letting $\eta_K \to \infty$ and thus $Re_\varepsilon \to 0$. In this limit Nir & Acrivos' (1973) analytical result (equation (3)) applies. A crude model for estimating $F^{n'}$ in the limit $a/\eta_K \to 0$ based on (3) is to determine the root-mean-square normal force for a randomly oriented doublet immersed in simple shear flow with $\dot{\gamma} = \sqrt{\bar{\varepsilon}/\nu}$. Applying (3) and averaging over all possible doublet orientations gives $F^{n'}\tau_K/(\mu a^2) = \frac{1}{4}\pi(h_1 + h_2) = 9.61$. This value is within the range of the intercept α as estimated from the linear fit. However, the model highly simplifies the situation in the sense that the spectrum of flow conditions experienced by the doublet is much richer than only simple shear.

An alternative and potentially more refined way to apply the Nir & Acrivos (1973) result to estimate forces in doublets in turbulent flow is to use the results of the simulations on the hydrodynamic environment of the doublet. For each time step during the various simulations we kept track of the rate-of-strain tensor averaged over a spherical volume around the centre of the doublet. These data together with the doublet orientation are substituted in (3) to determine at each time step the normal force in the doublet if it were immersed in a linear shear field with the instantaneous rate-of-strain tensor. As was already pointed out, since the doublet is usually larger than the Kolmogorov length scale, its hydrodynamic environment is non-homogeneous and a single rate-of-strain tensor around the doublet does not exist. The deviations between the actual force, and the force calculated via (3) are indicative of the role of inertia and of flow inhomogeneities around the doublet. The impact of the size of the averaging volume in determining the deformation rate around the doublet has been investigated; we present data for (spherical) averaging volumes with radius $3a$ and $2a$.

In figure 12 we show part of the time series we showed in figure 9 (*a*) along with the results from applying (3). There clearly is a correlation between the actual normal force signal and the ones modelled via (3). The correlation improves if we narrow the averaging volume from $3a$ to $2a$ radius, indicating that details regarding the flow around the doublet are important for the forces. However, peak levels of the actual signal are generally much larger than those based on modelling with (3) (note the different vertical scales in the panels of figure 12). Also, the higher frequency fluctuations in the actual signal are smoothed in the modelled signals. Figure 12(*c*) shows the level at which the centrifugal force contributes to F^n, and the way it fluctuates. A similar set of times series but now for a smaller a/η_K ratio are shown in figure 13. The picture changes quite drastically. The force as modelled with (3) now clearly follows the actual force much better. Peak levels of the modelled force time series are sometimes larger than those of the actual force.

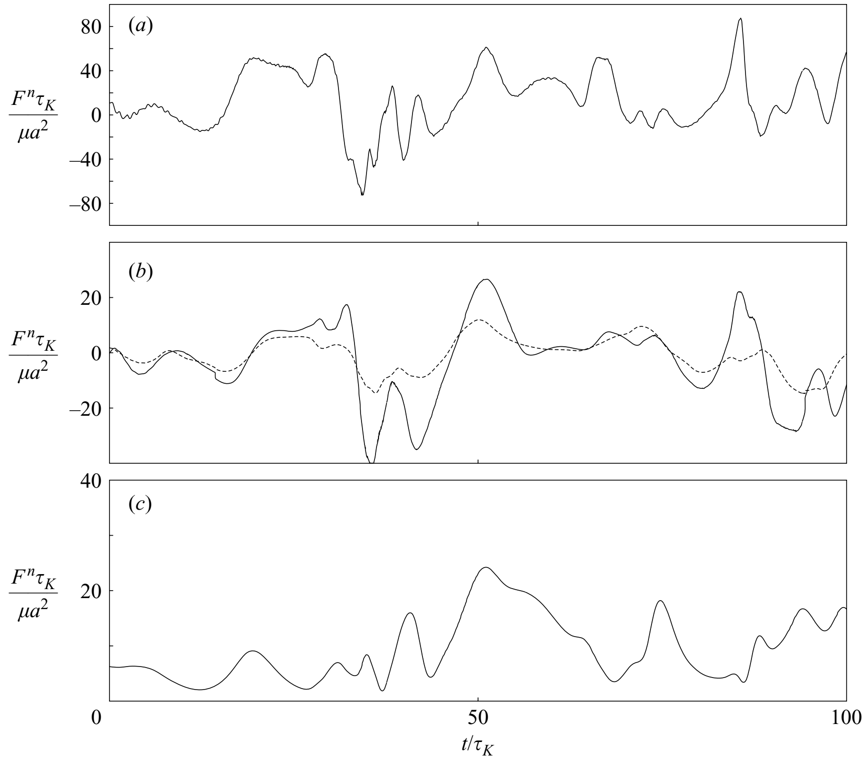

FIGURE 12. Time series of the normal force for the same case as figure 9 ($a/\eta_K = 8.3$, and $Re_{rms} = 27$). (*a*) Actual normal force time series; (*b*) normal force calculated by substituting in (3) the orientation of the doublet and the average rate-of-strain tensor around the doublet (solid line: averaging volume with radius $2a$, dashed line: averaging volume with radius $3a$); (*c*) contribution of the centrifugal force to the normal force.

In figure 14 we condense the modelled force data and plot them (similar to figure 11 for the actual force levels) as a function of a/η_K. The modelled force fluctuation levels (figure 14*b*) clearly depend on the size of the averaging domain around the doublet. Their trend with respect to a/η_K is opposite to the trend for the actual force fluctuation levels: a decrease for increasing a/η_K. Apparently, averaging the inhomogeneous flow around the doublet smooths out the details that induce high force levels, an effect that gets stronger as a/η_K increases, making modeling the interaction force in highly turbulent flow a difficult task. A similar remark applies to the average force. The modelled average force (figure 14*a*) decreases with increasing a/η_K; the actual average force increases (figure 11*a*).

4. Conclusions

Motivated by the potential role of fluid flow in breaking agglomerates we numerically investigated the force and torque required to maintain a fixed contact between equally sized solid spheres immersed in a flow. The direct numerical approach, which is based on solving the fluid flow by means of the lattice-Boltzmann method, was able to accurately reproduce the analytical results due to Nir & Acrivos (1973) for the case of a doublet in simple shear at creeping flow conditions. The minor deviations of the numerical from the analytical results could be largely attributed to

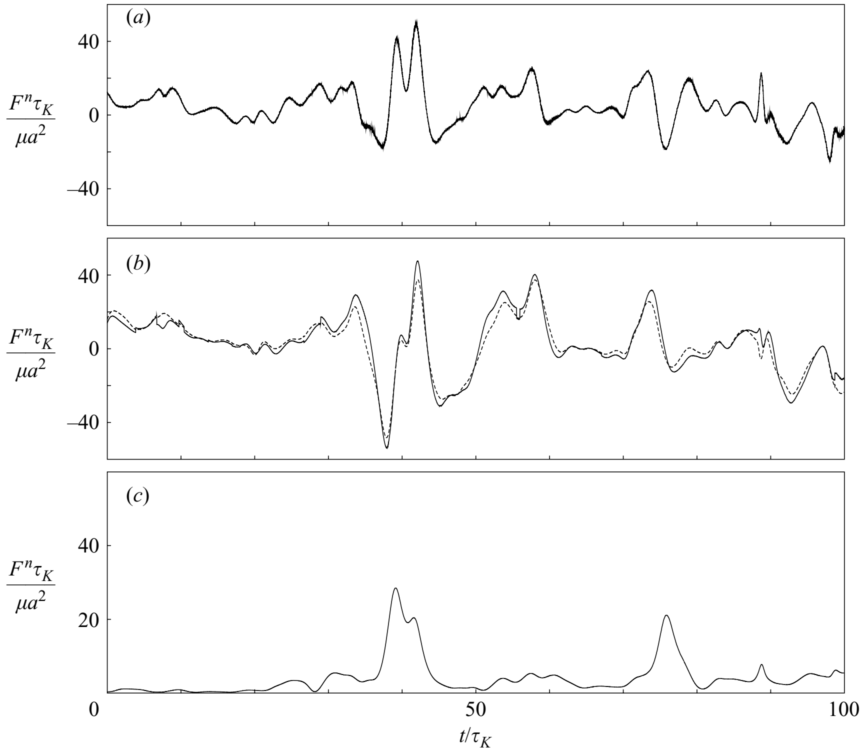

FIGURE 13. Same as figure 12, but for the case with $a/\eta_K = 2.1$, and $Re_{rms} = 4.1$.

physical effects: finite Reynolds number (including Saffman lift), domain size, and centrifugal force. The numerical results were virtually independent of the resolution of the simulations in the range $a = 6$ to 12, with a the sphere radius expressed in the number of grid spacings it spans.

After this validation study, the sphere doublet was immersed in turbulent flow. In a fully periodic domain, turbulence was generated by linear forcing. The force and torque to keep the two spheres attached now strongly fluctuates. The normal force peak levels typically are an order of magnitude higher than the maximum force attained if the doublet were immersed in a simple shear flow with $\dot{\gamma} = 1/\tau_K$ (with $\tau_K$the Kolmogorov time scale of the turbulent flow). On average the doublet experiences a tensile normal force. Partly, this is due to the centrifugal force always being tensile, and partly to the probability density function of radial relative velocity in turbulent flow being skewed, with its maximum at positive (separating) radial velocity.

The fluctuation levels of the normal force are generally larger than the average normal force, making the former more relevant for assessing doublet breakage. The fluctuation levels of the normalized normal interaction force have been shown to correlate with the ratio of sphere radius over Kolmogorov length scale a/η_K according to a linear relation. For a solid over fluid density ratio of 4.0 we found

$$\frac{F^{n'} \tau_K}{\mu a^2} = \alpha + \beta \frac{a}{\eta_K}$$

with $\alpha = 11 \pm 2$ and $\beta = 1.5 \pm 0.2$.

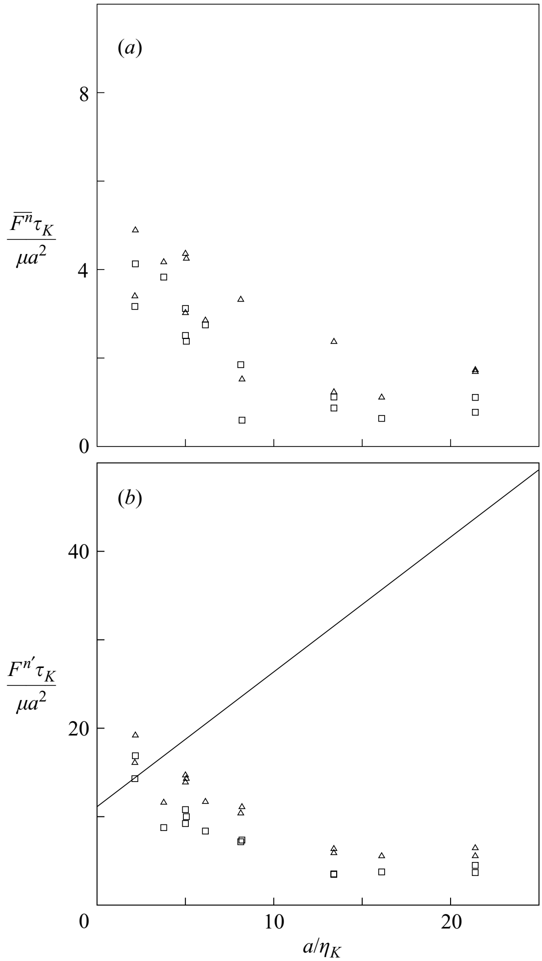

FIGURE 14. (*a*) The average ($\overline{F^n}$) and (*b*) root-mean-square normal force ($F^{n'}$) as estimated by means of (3) with the average deformation rate in the direct vicinity of the doublet. The square symbols relate to a spherical averaging volume with radius $3a$, the triangles one with radius $2a$. The line in (*b*) is (7) (see text).

The success of modeling the normal force in turbulent flow with Nir & Acrivos' (1973) analytical result depends highly on the size of the doublet in relation to the Kolmogorov length scale η_K. For roughly $a/\eta_K \leqslant 5$ the fluctuations levels of the normal force as estimated by means of the analytical result are comparable to the actual fluctuation levels. For higher a/η_K ratios, the agreement quickly deteriorates, caused by inertial effects and the inhomogeneity of the rate-of-strain tensor around the doublet.

Future work will focus on practical applications of the methodology developed here to assess flow-induced forces in agglomerates, a prominent one being the design of microfluidic layouts for effectively breaking agglomerates with specific bond strength. Also the solid over liquid density ratio (kept fixed at 4.0 in this study) deserves further attention. It plays a potentially complicated role. Heavier agglomerates will experience more centrifugal force on one side, and are less sensitive to quick changes in their hydrodynamic environment on the other. Furthermore we will consider bigger

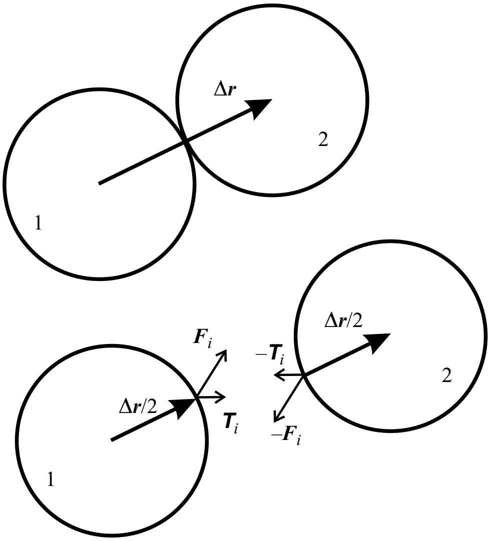

FIGURE 15. Definitions of interaction force $\boldsymbol{F}_i$, torque $\boldsymbol{T}_i$, and separation vector $\boldsymbol{\Delta r}$.

agglomerates (in terms of the number of primary particles), extending the parameter space with the morphology of agglomerates.

I thank one of the reviewers for pointing out me to the role of the Saffman lift force in the shear flow simulations, and an error in my derivation of the interaction torque.

Appendix. Derivation of interaction force and torque

The conditions for maintaining fixed contact between the two spheres forming the doublet are given by (1). In figure 15 we define the doublet geometry including the forces and torques acting at the point of contact.

The time derivative of the velocity of the contact point is a result of the linear acceleration of the sphere and the time derivative of the contribution from rotation of the sphere:

$$\frac{\mathrm{d}\boldsymbol{v}_{c1}}{\mathrm{d}t} = \frac{\mathrm{d}\boldsymbol{v}_{p1}}{\mathrm{d}t} + \frac{\mathrm{d}}{\mathrm{d}t}\left(\boldsymbol{\Omega}_{p1} \times \frac{1}{2}\boldsymbol{\Delta r}\right), \tag{A 1}$$

$$\frac{\mathrm{d}\boldsymbol{v}_{c2}}{\mathrm{d}t} = \frac{\mathrm{d}\boldsymbol{v}_{p2}}{\mathrm{d}t} - \frac{\mathrm{d}}{\mathrm{d}t}\left(\boldsymbol{\Omega}_{p2} \times \frac{1}{2}\boldsymbol{\Delta r}\right). \tag{A 2}$$

The linear acceleration of the spheres is due to the hydrodynamic force and the interaction force:

$$\frac{\mathrm{d}\boldsymbol{v}_{p1}}{\mathrm{d}t} = \frac{\boldsymbol{F}_{h1} + \boldsymbol{F}_i}{m} \quad \text{and} \quad \frac{\mathrm{d}\boldsymbol{v}_{p2}}{\mathrm{d}t} = \frac{\boldsymbol{F}_{h2} - \boldsymbol{F}_i}{m} \tag{A 3}$$

with m the mass of one sphere. $\boldsymbol{F}_{h1}$ and $\boldsymbol{F}_{h2}$ are known from the hydrodynamics part of the simulation procedure. Since $\mathrm{d}\boldsymbol{v}_{c1}/\mathrm{d}t = \mathrm{d}\boldsymbol{v}_{c2}/\mathrm{d}t$ and $\boldsymbol{\Omega}_{p1} = \boldsymbol{\Omega}_{p2} \equiv \boldsymbol{\Omega}_p$, subtracting (A 2) from (A 1), and substituting (A 3) leads to an expression for the interaction force:

$$\boldsymbol{F}_i = -\frac{1}{2}(\boldsymbol{F}_{h1} - \boldsymbol{F}_{h2}) - \frac{1}{2}m\frac{\mathrm{d}}{\mathrm{d}t}(\boldsymbol{\Omega}_p \times \boldsymbol{\Delta r}). \tag{A 4}$$

The angular acceleration $\mathrm{d}\boldsymbol{\Omega}_p/\mathrm{d}t$ is a result of the torques applied on the spheres. There are three contributions to the torque: (i) the hydrodynamic torque ($\boldsymbol{T}_{h1}$ for sphere 1, $\boldsymbol{T}_{h2}$ for sphere 2, both quantities being known from the hydrodynamics part of the simulation procedure), (ii) the torque induced by the interaction force (see figure 15), (iii) the interaction torque $\boldsymbol{T}_i$. For sphere 1:

$$I\frac{\mathrm{d}\boldsymbol{\Omega}_p}{\mathrm{d}t} = \boldsymbol{T}_{h1} + \frac{1}{2}\boldsymbol{F}_i \times \boldsymbol{\Delta r} + \boldsymbol{T}_i \tag{A 5}$$

For sphere 2:

$$I\frac{\mathrm{d}\boldsymbol{\Omega}_p}{\mathrm{d}t} = \boldsymbol{T}_{h2} + \frac{1}{2}\boldsymbol{F}_i \times \boldsymbol{\Delta r} - \boldsymbol{T}_i \tag{A 6}$$

with I the moment of inertia around the centre of the sphere ($I = \frac{2}{5}a^2m$).

Subtracting (A 6) from (A 5) directly gives an expression for the interaction torque:

$$\boldsymbol{T}_i = \frac{1}{2}(\boldsymbol{T}_{h2} - \boldsymbol{T}_{h1}). \tag{A 7}$$

In order to determine the interaction force from (A 4), the term

$$\frac{\mathrm{d}}{\mathrm{d}t}(\boldsymbol{\Omega}_p \times \boldsymbol{\Delta r}) = \frac{\mathrm{d}}{\mathrm{d}t}(\boldsymbol{\Omega}_p) \times \boldsymbol{\Delta r} + \boldsymbol{\Omega}_p \times \frac{\mathrm{d}}{\mathrm{d}t}(\boldsymbol{\Delta r})$$

needs to be determined. Adding (A 5) and (A 6) results in an expression for the angular acceleration:

$$\frac{\mathrm{d}\boldsymbol{\Omega}_p}{\mathrm{d}t} = \frac{1}{2I}(\boldsymbol{T}_{h1} + \boldsymbol{T}_{h2} + \boldsymbol{F}_i \times \boldsymbol{\Delta r}). \tag{A 8}$$

Furthermore

$$\frac{\mathrm{d}}{\mathrm{d}t}(\boldsymbol{\Delta r}) = \boldsymbol{\Omega}_p \times \boldsymbol{\Delta r}. \tag{A 9}$$

Substituting (A 8) and (A 9) in (A 4) gives

$$\boldsymbol{F}_i = -\frac{1}{2}(\boldsymbol{F}_{h1} - \boldsymbol{F}_{h2}) - \frac{1}{2}m\left[\frac{1}{2I}(\boldsymbol{T}_{h1} + \boldsymbol{T}_{h2} + \boldsymbol{F}_i \times \boldsymbol{\Delta r}) \times \boldsymbol{\Delta r} + \boldsymbol{\Omega}_p \times \left(\boldsymbol{\Omega}_p \times \boldsymbol{\Delta r}\right)\right]. \tag{A 10}$$

This equation can be cast in the form $\boldsymbol{A} \cdot \boldsymbol{F}_i = \boldsymbol{b}$ with $\boldsymbol{A}$ and $\boldsymbol{b}$ a known tensor and vector respectively. Solving for the three components of $\boldsymbol{F}_i$ then requires solving a linear 3 × 3 system.

REFERENCES

Chen, S. & Doolen, G. D. 1998 Lattice-Boltzmann method for fluid flows. *Annu. Rev. Fluid Mech.* **30**, 329–364.

Delichatsios, M. A. & Probstein, R. F. 1976 The effect of coalescence on the average drop size in liquid–liquid dispersions. *Ind. Engng. Chem. Fund.* **14**, 134–138.

Derksen, J. & Van den Akker, H. E. A. 1999 Large-eddy simulations on the flow driven by a Rushton turbine. *AIChE J.* **45**, 209–221.

Derksen, J. J. & Sundaresan, S. 2007 Direct numerical simulations of dense suspensions: wave instabilities in liquid-fluidized beds. *J. Fluid Mech.* **587**, 303–336.

Goldstein, D. Handler, R. & Sirovich, L. 1993 Modeling a no-slip flow boundary with an external force field. *J. Comput. Phys.* **105**, 354–366.

Gopalkrishnana, P., Manas-Zloczowera, I. & Fekeb, D. L. 2005 Investigating dispersion mechanisms in partially infiltrated agglomerates: Interstitial fluid effects. *Powder Tech.* **156**, 111–119.

Guerrero-Sanchez, C., Erdmenger, T., Ereda, P., Wouters, D. & Schubert, U. S. 2006 Water-soluble ionic liquids as novel stabilizers in suspension polymerization reactions: Engineering polymer beads. *Chemistry* A **12**, 9036–9045.

Hollander, E. D., Derksen, J. J., Portela, L. M. & Van den Akker, H. E. A. 2001 A numerical scale-up study for orthokinetic agglomeration in stirred vessels. *AIChE J.* **47**, 2425–2440.

Hounslow, M. J., Mumtaz, H. S., Collier, A. P., Barrick, J. P. & Bramley, A. S. A. 2001 Micro-mechanical model for the rate of aggregation during precipitation from solution. *Chem. Engng. Sc.* **56**, 2543–2552.

Kusters, K. A. 1991. The influence of turbulence on aggregation of small particles in agitated vessel. PhD. Thesis Eindhoven University of Technology, Netherlands.

Kwade, A. & Schwedes, J. 2002 Breaking characteristics of different materials and their effect on stress intensity and stress number in stirred media mills. *Powder Tech.* **122**, 109–121.

Ladd, A. J. C. 1994 Numerical simulations of particle suspensions via a discretized Boltzmann equation. Part 1. Theoretical foundation. *J. Fluid Mech.* **271**, 285–309.

Marchisio, D. L., Soos, M., Sefcik, & Morbidelli, M. 2006 Role of turbulent shear rate distribution in aggregation and breakage processes. *AIChE J.* **52**, 158–173.

Mody, N. A., Lomakin, O., Doggett, T. A., Diacovo, T. G. & King, M. R. 2005 Mechanics of transient platelet adhesion to von Willebrand factor under flow. *Biophys. J.* **88**, 1432–1443.

Nir, A. & Acrivos, A. 1973 On the creeping motion of two arbitrary-sized touching spheres in a linear shear field. *J. Fluid Mech.* **59**, 209–223.

Obermair, S., Gutschi, C., Woisetschläger, J. & Staudinger, G. 2005 Flow pattern and agglomeration in the dust outlet of a gas cyclone investigated by Phase Doppler Anemometry. *Powder Tech.* **156**, 34–42.

Overholt, M. R. & Pope, S. B. 1998 A deterministic forcing scheme for direct numerical simulations of turbulence. *Computers Fluids* **27**, 11–28.

Qian, Y. H. d'Humieres, D. & Lallemand, P. 1992 Lattice BGK for the Navier-Stokes equations. *Europhys. Lett.* **17**, 479–484.

Rosales, C. & Meneveau, C. 2005 Linear forcing in numerical simulations of isotropic turbulence: Physical space implementations and convergence properties. *Phys. Fluids* **17**, 095106.

Saffman, P. G. 1965 The lift on a small sphere in a slow shear flow. *J. Fluid Mech.* **22**, 385–400.

Saffman, P. G. 1968 Correction. *J. Fluid Mech.* **31**, 624.

Somers, J. A. 1993 Direct simulation of fluid flow with cellular automata and the lattice-Boltzmann equation. *Appl. Sci. Res.* **51**, 127–133.

Soos, M., Sefcik, J. & Morbidelli, M. 2006 Investigation of aggregation, breakage and restructuring kinetics of colloidal dispersions in turbulent flows by population balance modeling and static light scattering. *Chem. Engng. Sci.* **61**, 2349–2363.

Succi, S. 2001 *The Lattice Boltzmann Equation for Fluid Dynamics and Beyond*. Clarendon.

Ten Cate, A. Nieuwstadt, C. H., Derksen, J. J. & Van den Akker, H. E. A. 2002 PIV experiments and lattice-Boltzmann simulations on a single sphere settling under gravity. *Phys. Fluids* **14**, 4012–4025.

Ten Cate, A. Derksen, J. J. Portela, L. M. & Van den Akker, H. E. A. 2004 Fully resolved simulations of colliding spheres in forced isotropic turbulence. *J. Fluid Mech.* **519**, 233–271.

Wang, L. P., Wexler, A. S. & Zhou, Y. 2000 Statistical mechanical description and modelling of turbulent collision of inertial particles. *J. Fluid Mech.* **415**, 117–153.